Contents lists available at ScienceDirect

Biosensors and Bioelectronics

A bio-chemical application of N-GQDs and g-C$_3$N$_4$ QDs sensitized TiO$_2$ nanopillars for the quantitative detection of pcDNA3-HBV

CrossMark

Xuehui Pang[a], Hongjun Bian[b], Weijie Wang[a], Cheng Liu[a], Malik Saddam Khan[a], Qiao Wang[a], Jianni Qi[c], Qin Wei[a,*], Bin Du[a]

[a] *Key Laboratory of Chemical Sensing & Analysis in Universities of Shandong, University of Jinan, Jinan 250022, China*
[b] *Department of Emergency, Shandong Provincial Hospital Affiliated to Shandong University, Jinan 250021, China*
[c] *Central Laboratory, Shandong Provincial Hospital Affiliated to Shandong University, Jinan 250021, China*

ARTICLE INFO

ABSTRACT

Herein, TiO$_2$ nanopillars (NPs)/N-doped graphene quantum dots (N-GQDs)/g-C$_3$N$_4$ QDs heterojunction efficiently suppressed the photogenerated charges recombination and improved photo-to-current conversion efficiency. The introduced N-GQDs and g-C$_3$N$_4$ QDs could result in more effective separation of the photogenerated charges, and thus produce a further increase of the photocurrent. TiO$_2$ NPs/N-GQDs/g-C$_3$N$_4$ QDs were firstly applied as the photoactive materials for the fabrication of the biosensors, and the primers of pcDNA3-HBV were then adsorbed on the TiO$_2$ NPs/N-GQDs/g-C$_3$N$_4$ QDs modified electrode under the activation of EDC/NHS. With increase of the pcDNA3-HBV concentration, the photocurrent reduced once the double helix between the primers and pcDNA3-HBV formed. The developed photoelectrochemical (PEC) biosensor showed a sensitive response to pcDNA3-HBV in a linear range of 0.01 fmol/L to 20 nmol/L with a detection limit of 0.005 fmol/L under the optimal conditions. The biosensor exhibited high sensitivity, good selectivity, good stability and reproducibility.

1. Introduction

According to the GLOBOCAN 2012, primary liver cancer is the fifth leading cancer in men and is the ninth in women with 70–90% being hepatocellular carcinoma (HCC) (Jemal et al., 2011). Being one o.

f the most common infections worldwide, hepatitis B virus (HBV) is one of the major public health problems and the leading cause of HCC, and resulted in 686, 000 deaths per year (Mortality, 2015). HBV is a double-stranded DNA virus with an incomplete circular double-stranded DNA genome. According to more than 8% genetic variability in the full-length nucleotide sequence or 4–8% divergence in the S gene, at least 10 HBV genotypes (A to J) and their subtypes have been defined (Kurbanov et al., 2010; Tatematsu et al., 2009; Tran et al., 2008). The patients with active chronic hepatitis B have HBV DNA levels > 2000 IU/mL with fluctuations that reach > 20,000 IU/mL in some patients. The peripheral blood of the patient is infectious, and HBV has the intact HBV genomic sequence and has been applied for the research on the influence on hepatic cell and other cells. HBV can effectively transcribe, translate and express the related protein in the cell, which totally reflect the real status of HBV *in vivo*. It can reflect the monitor effect to HBV itself from another aspect by detecting the

HBV DNA (Baker et al., 2015). Therefore, it is very significant to detect HBV for the early warning of HCC. Here, a visible light induced PEC platform based on TiO$_2$ NPs/N-GQDs/g-C$_3$N$_4$ QDs for the detection of HBV was proposed.

Since g-C$_3$N$_4$ was reported because of its visible-light photocatalytic performance in 2008 (Carlsson, 2008), it is regarded as a new metal-free and robust organic semiconductor, which has been widely used benefiting from its thermal, electrical and optical characteristics (Cao et al., 2015; Hong et al., 2016; Wang et al., 2014a). However, the application of bulk g-C$_3$N$_4$ was greatly limited due to the relatively small specific surface area, low photoresponsivity and poor solubility, *etc.* (Ma et al., 2014). To solve these problems, many attempts have been focused on preparing different morphologies of nanostructured g-C$_3$N$_4$, such as quantum dots (QDs) (An et al., 2016; Li et al., 2016; Zhang et al., 2014b; Zou et al., 2016), nanosheets (Duan et al., 2015; Han et al., 2016) or nanospheres (Jun et al., 2013; Zhang et al., 2014a), *etc.* g-C$_3$N$_4$ QDs have a wider band gap and present superior catalytic activity as the conduction and valence bands (CB and VB) shift in opposite directions owing to the quantum effect (Zhou et al., 2015b). g-C$_3$N$_4$ QDs have also looked as a potential candidate of carbon-based QDs with more unique photoluminescence (PL) properties than other

carbon-based QDs. These indicate that g-C_3N_4 QDs could act as a good co-catalyst for the semiconductor catalysts. Nevertheless, to date, there are few reports about their application in the biosensing fields (Ding et al., 2016; Feng et al., 2016; Li et al., 2014a, 2014b; Liu et al., 2016; Wang et al., 2013a, 2013b; Wang et al., 2016b, 2016c). Thus, in this work, g-C_3N_4 QDs were used to sensitize the PEC exitons transmission between TiO_2 and g-C_3N_4 QDs.

Graphene quantum dots (GQDs) are a hot newcomer of graphene family (Pan et al., 2010; Yan et al., 2010b). GQDs are carbon nanosheets of < 20 nm in lateral dimension and a quasi-zero-dimensional graphene material with a tuned band gap. It attracted great research attention recently because of its quantum confinement, edge effects (Li et al., 2011; Ponomarenko et al., 2008), excellent photoluminescence property (Yoon et al., 2016) in electronics (Bae et al., 2010; Lalwani et al., 2014), and biofields (Li et al., 2013; Peng et al., 2012; Wang et al., 2016a; Zhu et al., 2012), and so on. Due to its photon down conversion property, which could absorb photons in shorter wavelength regions and emit photons in longer wavelength regions, they have been implemented in bandgap applications recently (Liu et al., 2013a, 2013b; Tetsuka et al., 2016; Tsai et al., 2015). Owing to the high surface area, GQDs have the potential to be an ideal loading platform for various molecules (Abdullah-Al-Nahain et al., 2013; Wang, 2013) through covalent or noncovalent interaction in versatile biomedical applications (Zhang et al., 2013). The abundant functional groups, such as carboxyl, hydroxyl and epoxy groups on GQDs, endow them with good dispersion in water. In addition, compared with most of II–VI materials which contain some toxic elements, GQDs are nontoxic, environmentally friendly and reasonably biocompatible, which are favorable in practical applications. Considered the merits above, GQDs are a perfect photosensitizer for the specific activation of TiO_2.

As we know, TiO_2 is a most widely used semiconductor since Fujishima and Hondal reported TiO_2 as the semiconductor photoanode illuminated by ultraviolet light (Fujishima and Honda, 1972). Nevertheless, the intrinsic wide bandgap of TiO_2 (~3.2 eV) means the poor visible light absorption and poor photo-to-current ability under the visible light illumination. In this work, g-C_3N_4 QDs and N-GQDs were utilized to sensitize TiO_2 to achieve stronger visible light absorbency by forming the offsets, which would be advantageous to control the electrical transport of carriers. Futhermore, the primers were used as the capture probes for HBV with pcDNA3 vector. Thus, a biosensor based on PEC method was developed for the pcDNA3-HBV detection as shown in Scheme 1. This PEC biosensor might offer a candidate method for pcDNA3-HBV.

2. Experimental

2.1. Preparation of TiO_2 NPs

TiO_2 NPs were prepared as reported before with slight modification (Zhou et al., 2015a). 3 g of degussa P25 TiO_2 was dispersed in 160 mL of NaOH solution (5 mol/L) with stirring for 15 min. Then the mixture was sealed in a 200 mL Teflon-lined stainless steel autoclave for 24 h at 200 °C. Then the precipitate was transferred into 250 mL of HCl solution (10%, v/v) with magnetic stirring for 10 h. After filtering and washing with the ultrapure water for 5 times, the precipitate was dried and calcined at 700 °C in air for 3 h.

2.2. Preparation of N-GQDs

N-GQDs were prepared as described before (Zou et al., 2016). Typically, 0.3003g carbamide and 0.2627g citric acid were mixed in 6 mL ultrapure water, and then stirred to obtain a clear solution. The solution was put into the Teflon autoclave (50 mL), and then was heated at 160 °C for 8 h. The solution was centrifuged at 5000 rpm for 5 min and the final product was obtained.

2.3. Preparation of g-C_3N_4 QDs

Bulk g-C_3N_4 was obtained as previously (Pang et al., 2015). 10 g of melamine powder was put into a covered ceramic crucible and heated in a muffle furnace for 4 h at 550 °C. Bulk g-C_3N_4 was obtained after naturally cooling to room temperature. g-C_3N_4 QDs were prepared according to the literature (Wang et al., 2014b). Bulk g-C_3N_4 powders were heated at 500 °C in an open ceramic container with a ramp rate of 2 °C/min for 2 h. The obtained powder was mixed with 40 mL of concentrated H_2SO_4 and 120 mL of HNO_3 with drastic ultrasonication for 18 h. Then, the obtained solution was diluted with 800 mL of ultrapure water to form a colloidal suspension to obtain g-C_3N_4 nanosheets through a microfilter (0.45 μm) (Fig. 1G). g-C_3N_4 nanosheets were redispersed under ultrasonication in 20 mL ultrapure water. The suspension was placed into a Teflon autoclave (100 mL) and heated for 10 h at 200 °C. After cooling to room temperature, g-C_3N_4 QDs was obtained through filtering with a 0.22 μm microfilter.

2.4. Preparation of pcDNA3-HBV and PCR

pcDNA3-HBV DNA was obtained from Central Laboratory of Shandong Provincial Hospital Affiliated to Shandong University. HBV DNA with a pcDNA3 vector was transfected into the JM109. And the JM109 was cultured at 37 °C for 16 h to vastly amplify this plasmid.
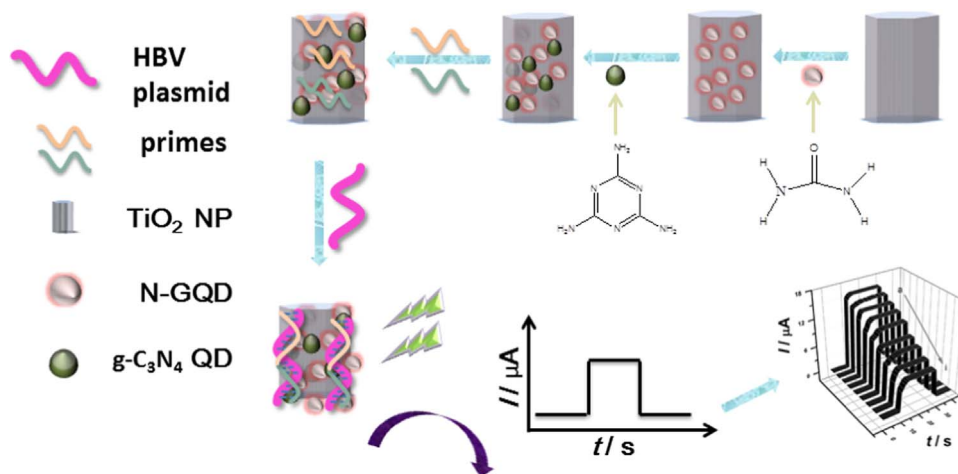
Scheme 1. Schematic illustration of the PEC biosensor fabrication procedure.
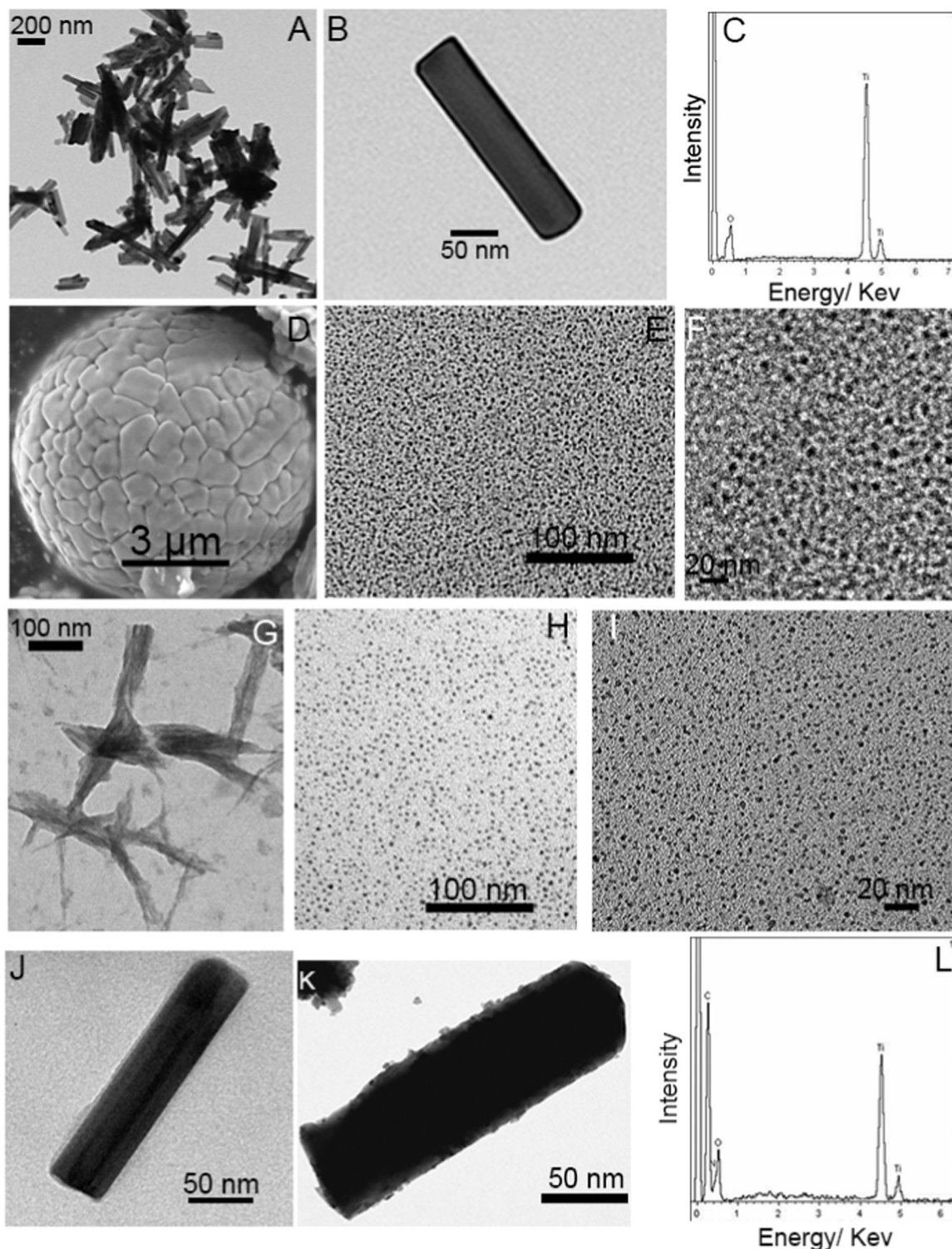
Fig. 1. TEM images of TiO$_2$ NPs (A, B), g-C$_3$N$_4$ nanosheets (G), TiO$_2$ NPs/N-GQDs (J) and TiO$_2$ NPs/N-GQDs/g-C$_3$N$_4$ QDs (K); SEM image of N-GQDs (D); HRTEM images of N-GQDs (E, F) and g-C$_3$N$_4$ QDs (H, I); EDS of TiO$_2$ NPs (C) and TiO$_2$ NPs/N-GQDs/g-C$_3$N$_4$ QDs (L).

Next, the pcDNA3-HBV was extracted with nucleic acid purification kit (Catalog #: AP-MM-P-50, Axygen scientific, Central Avenue, Union City, USA) according to the manufacturer's instructions. The pcDNA3-HBV plasmid was used as a template for PCR using Ex Taq (Catalog #: RR001A, TaKaRa, Development Zone, Dalian, China), according to the manufacturer's protocol. Specific primers used for PCR assays were as follows: 5′-ATGGA CATTG ACCCG TAT-3′ (sense), 5′-CTAAC ATTGA GATTC CCGAG-3′- (antisense) for Primer Pairs-1, and 5′-TGAAT CCTGC GGACG ACC-3′-(sense), 5′-CAGCT TGGAG GCTTG AACAG-

3′- (antisense) for primer Pairs-2. PCR was performed according to the following steps: 95 °C for 5 min, followed by 40 cycles of 95 °C for 5 s, 56 °C for 5 s, 72 °C for 5 s and 72 °C for 5 min, using the ABI Veriti$^@$ −96 PCR System.

2.5. Fabrication of the PEC biosensor

Scheme 1 displayed the fabrication process of the developed PEC biosensor. Firstly, 5 µL of nanohybridization of TiO$_2$ NPs (15 mg/mL)

were deposited on the bare ITO electrode. Secondly, 5 µL of N-GQDs (18 mg/mL) were deposited on TiO_2 NPs/ITO electrode with EDC/ NHS. Thirdly, 5 µL of g-C_3N_4 QDs (20 mg/mL) were deposited on TiO_2 NPs/g-C_3N_4 QDs/ITO electrode with EDC/NHS. Then, 8 µL of primers (15 g/mL) were deposited on TiO_2 NPs/g-C_3N_4 QDs/N-GQDs/ITO electrode with EDC/NHS and incubated at 4 °C for 5 h. Finally, 1 mL of the different concentrations of pcDNA3-HBV were deposited on 3′ and 5′ primers/TiO_2 NPs/g-C_3N_4 QDs/N-GQDs/ITO electrode surface respectively and incubated at 4 °C for 5 h.

2.6. Measurement procedure

PEC and EIS tests were performed immediately on an electrochemical work station (Zahner Zennium PP211, Germany) after finishing the incubation of pcDNA3-HBV with an irradiation wavelength of 430 nm at 25 °C. Phosphate buffered solution containing 0.1 mol/L of ascorbic acid (AA) was the electrolyte solution. 0.1 V was used the bias voltage. Light duration was 20 s and no light duration was 10 s. A three-electrode system was used (the working electrode was the modified ITO electrode, the reference electrode was a saturated calomel electrode (SCE) and the auxiliary electrode consisted of a platinum wire).

3. Results and discussion

3.1. Characterization of TiO_2 NPs, g-C_3N_4 QDs and N-GQDs

Fig. 1A and B showed the transmission electron microscope (TEM) morphologies of as-prepared dispersed TiO_2 NPs with almost average diameter. TEM was usually used to reveal the small size of the prepared material from JEM-1400 (JEOL, Japan). It can be seen that TiO_2 NPs were independent and Fig. 1B showed a single TiO_2 NP with a perfect pillar shape. EDS result in Fig. 1C displayed only two kinds of elements of Ti and O, which further proved the successful preparation of TiO_2. Fig. 1D showed the scanning electron microscope (SEM) morphology of macro-collective N-GQDs. SEM image was obtained from JSM-6700F microscope (JEOL, Japan). It can be seen N-GQDs gathered as a microsphere with some micro-ravine. Fig. 1E and F described the TEM and HRTEM morphologies of the dispersive QDs, which showed the abundance of N-GQDs and their size was about 100 nm and 20 nm. HRTEM images were collected from a JEM-2100F microscope (JEOL, Japan). Fig. 1G showed the TEM morphology of the prepared g-C_3N_4 nanosheets during the preparation step of g-C_3N_4 QDs. Fig. 1H and I showed the TEM and HRTEM morphologies of the prepared g-C_3N_4 QDs. The output was plentiful with a uniform diameter, which verified

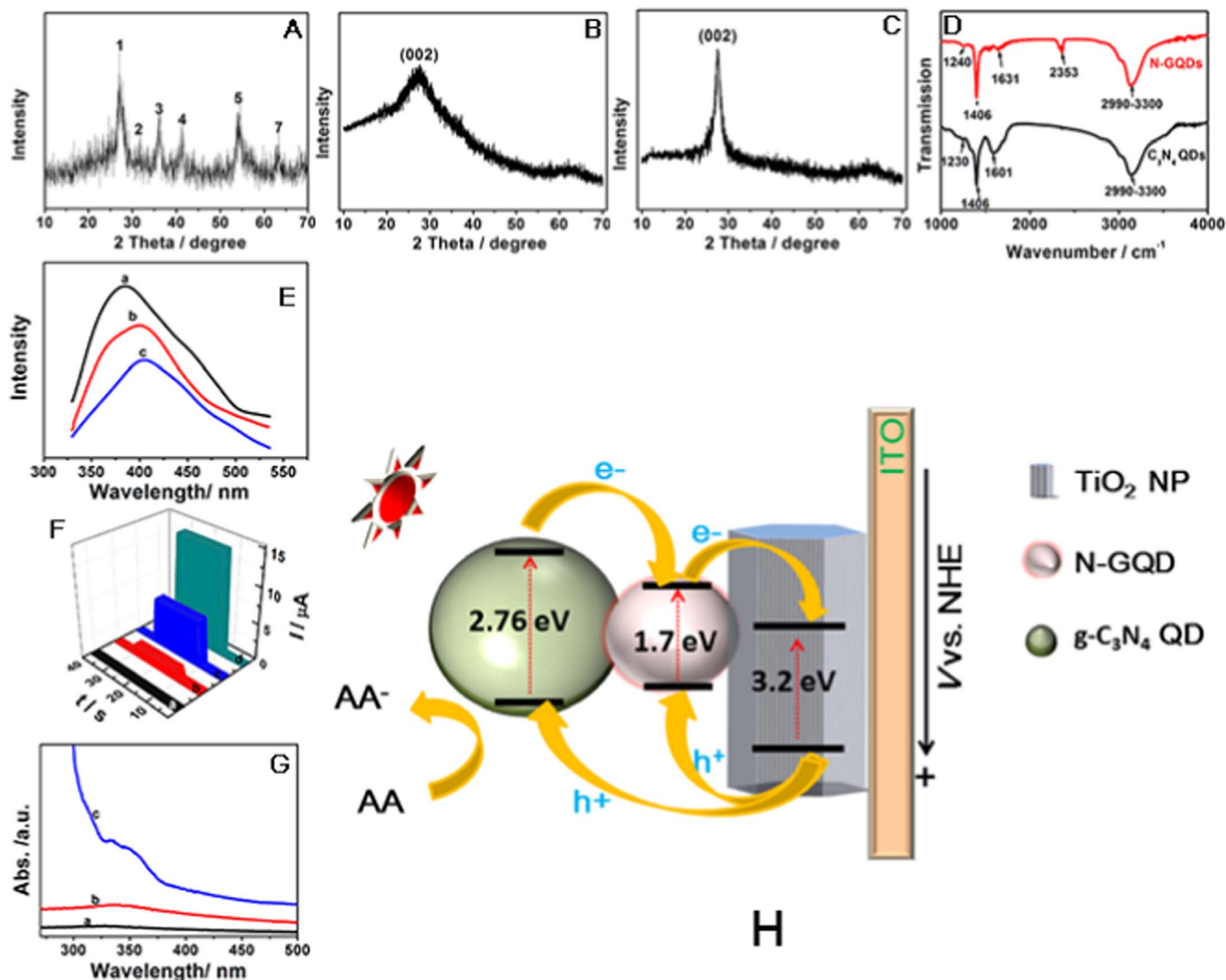**Fig. 2.** XRD patterns of TiO_2 NPs (A) N-GQDs (B) and g-C_3N_4 QDs (C); FT-IR spectra (D) of N-GQDs (above) and g-C_3N_4 QDs (bottom); PL emission spectra(E) of (a) TiO_2 NPs, (b) TiO_2 NPs/N-GQDs and (c) TiO_2 NPs/N-GQDs/g-C_3N_4 QDs, time-based photocurrent responses (F) of (a) ITO, (b) TiO_2 NPs, (c) TiO_2 NPs/N-GQDs and (d) TiO_2 NPs/N-GQDs/g-C_3N_4 QDs and UV–vis spectra (G) of (a) TiO_2 NPs, (b) TiO_2 NPs/N-GQDs and (c)TiO_2 NPs/N-GQDs/g-C_3N_4 QDs; (H) Schematic illustration of the energy level diagram.

that the preparation met the requirement. Fig. 1J and K exhibited the TEM morphologies of the TiO$_2$ NPs/N-GQDs and TiO$_2$ NPs/N-GQDs/g-C$_3$N$_4$ QDs nanocomposites. It can be seen that the N-GQDs covered as a semitransparent chiffon in Fig. 1J. However, after g-C$_3$N$_4$ QDs hybridized with TiO$_2$ NPs/N-GQDs, the coating was so thick that some QDs aggregated like some granulums on the surface in Fig. 1K. EDS result in Fig. 1L showed that four kinds of elements, Ti, O, C and N, which suggested the perfect hybridization of TiO$_2$ NPs, N-GQDs and g-C$_3$N$_4$ QDs in the final sample.

Fig. 2A showed XRD patterns of TiO$_2$ NPs, g-C$_3$N$_4$ QDs and N-GQDs respectively. XRD patterns were collected by D8 focus diffractometer (Bruker AXS, Germany). Seven diffraction peaks can be distinguished, which respectively corresponded to (110), (101), (111), (210), (211), (220) and (002) plane indexed from 1 to 7. In Fig. 2B, a broad peak at about 26.5° was (002) plane, whose d value of 0.389 nm was nearly same with that of graphene (Pang et al., 2016). This result suggested that N-GQDs owned plentiful oxygen-containing functional groups (Liu et al., 1996; Peng et al., 2012). Fig. 2C displayed XRD pattern of g-C$_3$N$_4$ QDs. The peak at about 27.6° can be assigned to (002) plane with a distance of 0.325 nm and (100) peak almost disappeared due to the carboxyl measurement by H$_2$SO$_4$ and HNO$_3$ (Pang et al., 2015). These results showed that the carboxyl process did not influence the lattice structure of g-C$_3$N$_4$ QDs and benefited for the following fabrication of the biosensor.

Fig. 2D showed Fourier Transform Infrared (FT-IR) spectra of N-GQDs and g-C$_3$N$_4$ QDs from 1000 to 4000 cm^{-1}. FT-IR spectra were obtained from a Perkin-Elmer 580B spectrophotometer (Perkin-Elmer, USA). The above and bottom lines referred to FT-IR spectra of N-GQDs and g-C$_3$N$_4$ QDs respectively. For N-GQDs, the peak at 1240 cm^{-1} might be the stretching vibrations of C-N bond, and the stretching vibrations of C-N bond may associate to 1251 cm^{-1} for g-C$_3$N$_4$ QDs. C$^=$O bending vibrations of both of the two nanomaterials located at the sharp peak at about 1406 cm^{-1}. C-O band stretching vibrations may be corresponded to the peaks centering at about 1631 (above) and 1601 (bottom) cm^{-1} in both lines. The peak locating at 2353 cm^{-1} might be associated to the stretching vibrations of cumulated double bonds. The broad peaks in both lines from about 2990–3300 cm^{-1} were assigned to C-H and N-H bonds stretching vibrations. FT-IR data indicated that N-GQDs and g-C$_3$N$_4$ QDs loaded lots of functional groups of carboxyl groups and amino groups, which would be in favor of the biocompatibility and hydrophilicity in aqueous system for the detection process.

3.2. The proposed mechanism of PEC performance enhancement

Fig. 2H schematically illustrated the PEC promotion mechanism of the photo-to-electron generator of TiO$_2$ NPs/N-GQDs/g-C$_3$N$_4$ QDs. From Fig. 2H, it can be seen that the relative Fermi level alignment formed among TiO$_2$ NPs, N-GQDs and g-C$_3$N$_4$ QDs. As we know, the band gap of TiO$_2$, N-GQDs and g-C$_3$N$_4$ QDs is about 3.2 eV, 1.7 eV and 2.76 eV, respectively. The CB edge potential of TiO$_2$ is about −0.44 V (*vs.* normal hydrogen electrode, NHE) (Kanan and Nocera, 2008; Yin et al., 2009). Those of N-GQDs and g-C$_3$N$_4$ QDs are about −0.94 V (Gupta et al., 2011; Zhang et al., 2011) and −1.12 V (*vs.* NHE) (Ge et al., 2011; Yan et al., 2010a), respectively. Then, it can be calculated that VB of TiO$_2$, N-GQDs and g-C$_3$N$_4$ QDs are 2.76 V, 0.76 V and 1.64 V (*vs.* NHE) respectively according to $E_g = V_{VB} - V_{CB}$. In addition, it can be deduced that VB and CB energy level of TiO$_2$ NPs located below those of N-GQDs and g-C$_3$N$_4$ QDs. And also the CB energy level of g-C$_3$N$_4$ was negative than that of N-GQDs. While exposed under the visible light, the photogenerated electrons of g-C$_3$N$_4$ QDs and N-GQDs were excited, and then transferred quickly from the VB to the CB. Moreover, the photogenerated electrons excited from g-C$_3$N$_4$ can be easily injected into N-GQDs because of different CB energy levels. And after that, these electrons excited from g-C$_3$N$_4$ QDs and N-GQDs could be easily injected into the CB of TiO$_2$ NPs. Still further, the separated holes on VB of TiO$_2$ can enter into g-C$_3$N$_4$ and N-GQDs, which

transmission benefited for the PEC performance. And the holes would be transmitted to the interface between the electrode and the electrolyte, and be reduced by AA in the electrolyte to improve the charge transfer and separation efficiency as described in Fig. 2H (Gao et al., 2015). The above illustration explained that g-C$_3$N$_4$ QDs and N-GQDs can improve the visible light absorption property of TiO$_2$ NPs and this phenomenon was also proved by the results of PL, PEC and UV–vis as follows.

As we know, stronger photoluminescence (PL) value currently meant weaker photocatalytic intensity for the semiconductors (Cheng et al., 2014). Thus, in this work, PL tests were carried out to inspect the PEC behavior of TiO$_2$ NPs, TiO$_2$ NPs/N-GQDs and TiO$_2$ NPs/g-C$_3$N$_4$ QDs/N-GQDs nanocomposites. LS-45/55 PL spectrometer (Perkin Elmer, USA) was used to collect the PL spectra. In Fig. 2E, curve (a) showed an apparent higher PL emission intensity of TiO$_2$ NPs. And PL intensity in curve (b) turned lower when N-GQDs were deposited on the electrode. After modified with g-C$_3$N$_4$ QDs, PL intensity turned much lower than those of TiO$_2$ NPs and TiO$_2$ NPs/N-GQDs. As the PL tests results shown, the combination of TiO$_2$ NPs, N-GQDs and g-C$_3$N$_4$ QDs made the lower recombination efficiency of the photogenerated e$^-$/h$^+$ pairs, which indicated higher electron injection efficiency. These results proved that the viewpoint illustrated in Fig. 2H, the sensitization of N-GQDs and g-C$_3$N$_4$ QDs to TiO$_2$ NPs can improve the photoelectron transfer and be valued for the photoelectrons transformation, was probable.

Fig. 2F showed the time-based photocurrent responses of TiO$_2$ NPs, TiO$_2$ NPs/N-GQDs and TiO$_2$ NPs/N-GQDs/g-C$_3$N$_4$ QDs. Curve (a) showed there was no response on ITO electrode and curve (b) showed TiO$_2$ NPs owned the poor absorption property in the visible light because of its wide band gap. The combination and sensitization of N-GQDs made the photocurrent apparently increased (curve c) and the photocurrent further enhanced after modified g-C$_3$N$_4$ QDs (curve d). This phenomenon maybe prove that g-C$_3$N$_4$ QDs and N-GQDs can benefit efficiently for the electron injection between VB and CB and effectively suppressed h$^+$/e$^-$ pairs recombination.

UV–vis was also applied to inspect PEC properties and the absorption spectra of TiO$_2$ NPs, TiO$_2$ NPs/N-GQDs and TiO$_2$ NPs/N-GQDs/g-C$_3$N$_4$ QDs. The spectra were all obtained from Lambda 35 UV–vis spectrometer (Perkin-Elmer, USA). As shown in Fig. 2G (curve a), TiO$_2$ NPs exhibited a very weak light absorption in the visible light due to its wide band gap. Curve (b) displayed a higher light absorption between 320–350 nm, suggesting that N-GQDs increased the light absorption ability of the nanocomposite (TiO$_2$ NPs/N-GQDs). Moreover, a slight apparently absorption hill from 330 to 370 nm appeared in curve (c) (TiO$_2$ NPs/N-GQDs/g-C$_3$N$_4$ QDs), which was ascribed to the sensitization of N-GQDs and g-C$_3$N$_4$ QDs. These results could prove that the addition of N-GQDs and g-C$_3$N$_4$ QDs improved the absorbency of TiO$_2$ in the visible light, which improved the practical applications in the future.

3.3. Characterization of the proposed biosensor

As an effective tool to characterize the interface property of the electrodes, EIS was applied to test the fabrication procedure of the PEC biosensor. Fig. 3A displayed the Nyquist plots with different modification processes with [Fe(CN)$_6$]$^{3-/4-}$ as the redox probe. As we know, the electron-transfer resistance (R_{et}), which equals the semicircle diameter at higher frequencies, reflects the restricted diffusion of the redox probe through the multilayer system related directly to film permeability. The linear portion at lower frequencies corresponds to the diffusion-limited process. After modification by TiO$_2$ NPs, R_{et} increased, as shown in curve (a), which was due that the deposition of TiO$_2$ NPs increased the impedance. Then, the immobilization of g-C$_3$N$_4$ QDs and N-GQDs leaded to further R_{et} enhancement in curve (b) and c, which resulted from the hindered interfacial electron transfer. Finally, after being incubated with the primers, R_{et} got higher as the forming of
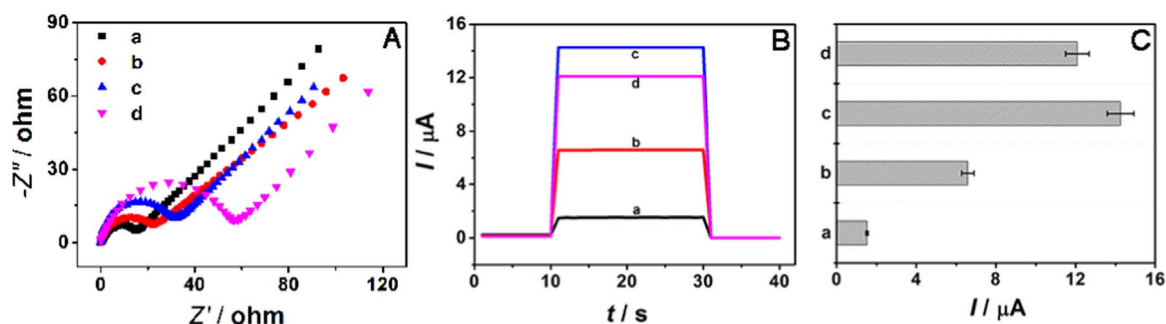
Fig. 3. (A)EIS spectra and (B)time-based photocurrent responses of (a) TiO$_2$ NPs/ITO, (b) TiO$_2$ NPs/N-GQDs/ITO and (c)TiO$_2$ NPs/N-GQDs/g-C$_3$N$_4$ QDs/ITO (d) 3'and 5' primers/ TiO$_2$ NPs/N-GQDs/g-C$_3$N$_4$ QDs/ITO.
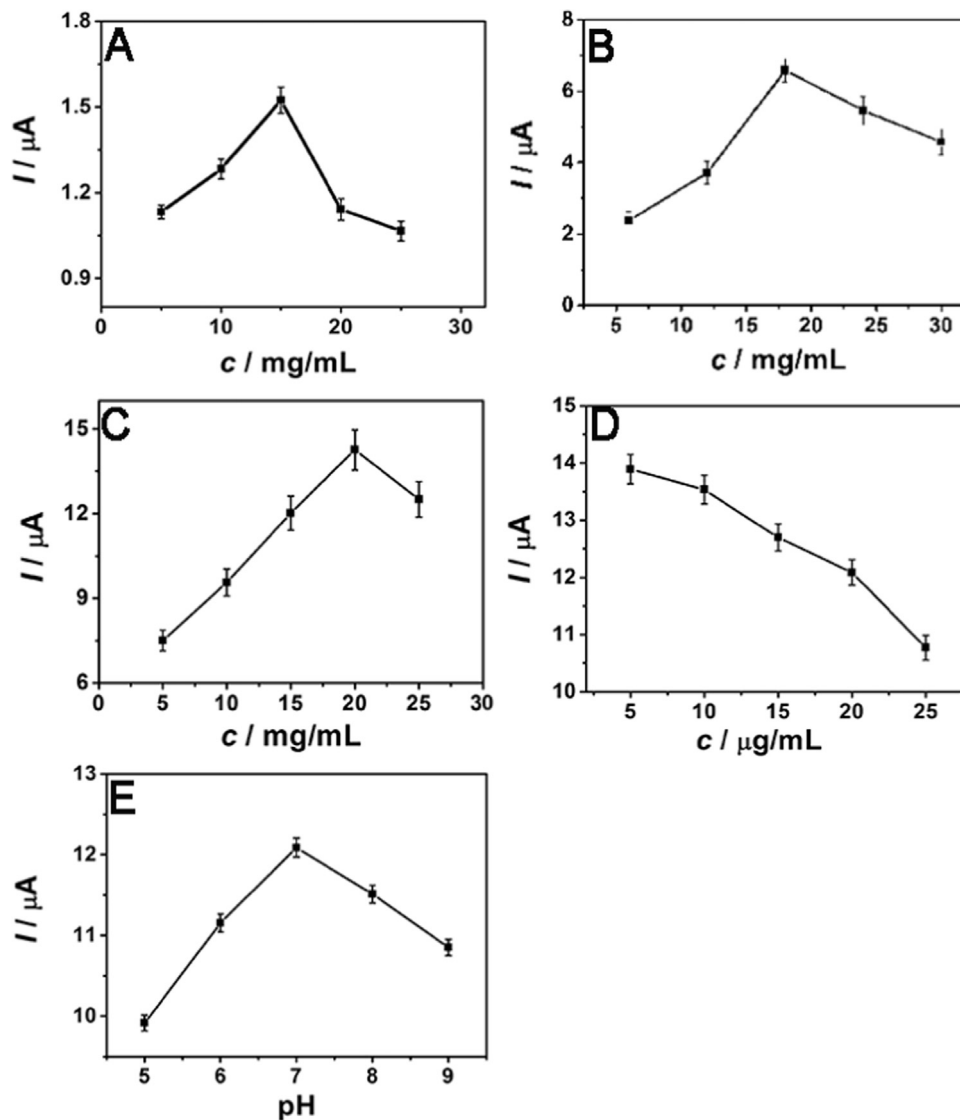

Fig. 4. The optimization of experimental conditions by time-based photocurrent responses of the concentrations of TiO$_2$ NPs (A), N-GQDs (B), g-C$_3$N$_4$ QDs (C), the primers (D); pH after modifying TiO$_2$ NPs/N-GQDs/g-C$_3$N$_4$ QDs/ITO (E).

bioaffinity complexes which further hindered the electron transfer. The above results displayed every successful fabrication step.

The fabrication process was also monitored as shown in Fig. 3B and C by PEC method. As for curve a-c, the photocurrent obviously increased benefiting from the good visible-light response after modified TiO$_2$ NPs, g-C$_3$N$_4$ QDs and N-GQDs layer by layer on the electrode. This could be attributed to the fact that the nanocomposite of TiO$_2$ NPs/N-GQDs/g-C$_3$N$_4$ QDs suppressed the interfacial electron transfer

and partly obstructed electron donor to the surface reaction with the photogenerated hole. After that, the photocurrent gradually decreased with the immobilization of the bio-anchorer, namely "the primers" (curve d). This phenomenon was ascribed to the electrostatic repulsion of negative charged backbone of DNA fragments. The above results indicated that the fabrication of the sensing interface was successful.
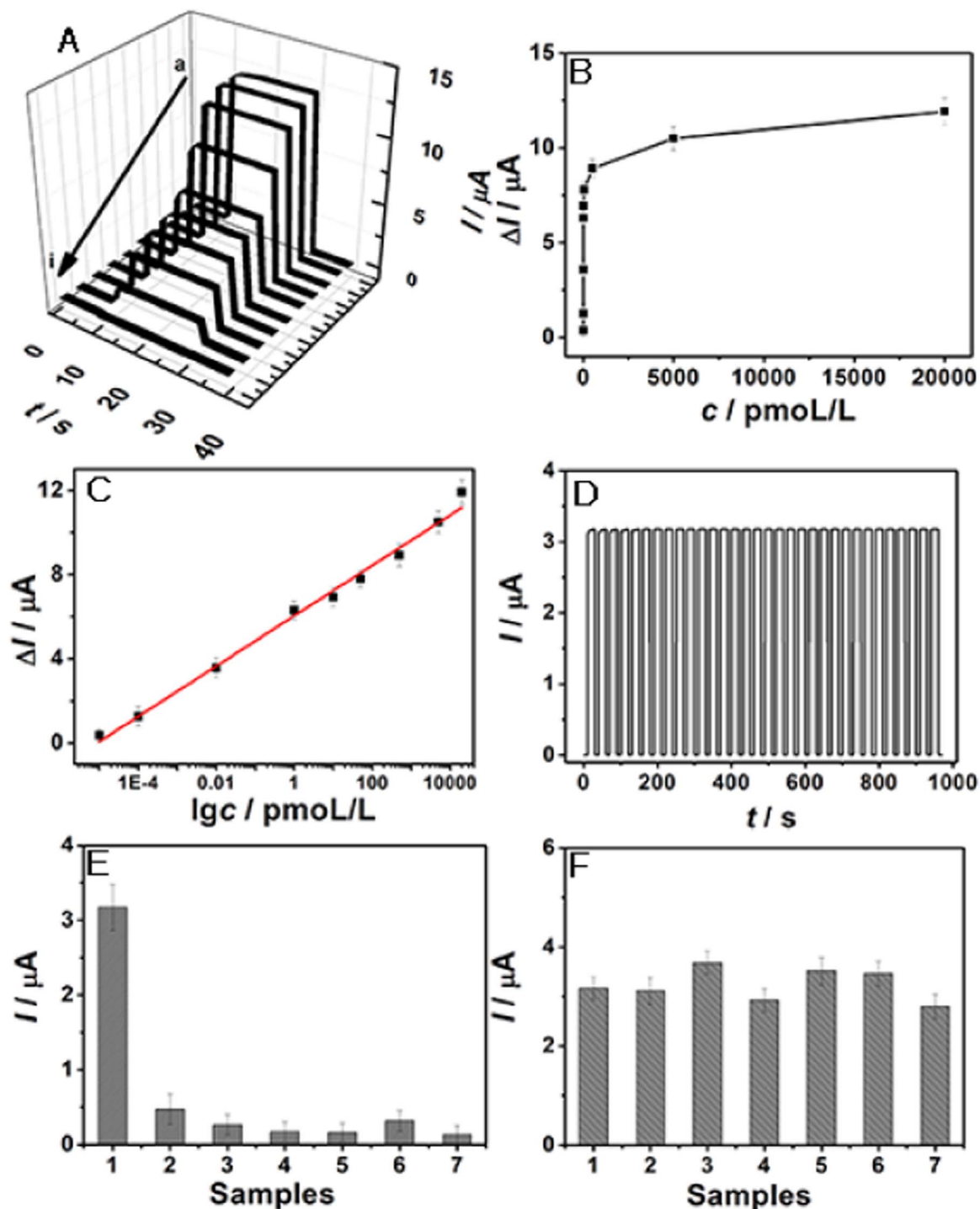
Fig. 5. (A) Time-based photocurrent responses of being incubated with different concentrations of pcDNA3-HBV; (B) Relation curve between photocurrent change (ΔI) and different pcDNA3-HBV concentrations; (C) Logarithmic calibration curve between ΔI and concentration of pcDNA3-HBV; (D)Stability of photocurrent response under the optimal condition; (E) Selectivity of the biosensor (1) 500 pmol/L pcDNA3-HBV, (2) 500 pmol/L pcDNA3, (3) 500 pmol/L pcDNA3-His, (4) 500 pmol/L pCMV5, (5) 500 pmol/L pCMV-N-HA, (6) 500 pmol/L pCMV-C-HA and (7) five kinds of gene fragments of 1000 pmol/L respectively; (F) Selectivity of the biosensor (1) 500 pmol/L pcDNA3-HBV, (2) 500 pmol/L pcDNA3-HBV +1000 pmol/L pcDNA3, (3) 500 pmol/L pcDNA3-HBV +1000 pmol/L pcDNA3-His, (4) 500 pmol/L pcDNA3-HBV +1000 pmol/L pCMV5, (5) 500 pmol/L pcDNA3-HBV +1000 pmol/L pCMV-N-HA, (6) 500 pmol/L pcDNA3-HBV +1000 pmol/L pCMV-C-HA and (7) 500 pmol/L pcDNA3-HBV + five kinds of gene fragments of 1000 pmol/L respectively.

3.4. PEC detection of pcDNA3-HBV

In order to gain the good detecting effect, the experiment condition optimization was carried out. The optimal concentrations of TiO$_2$ NPs (Fig. 4A), N-GQDs (Fig. 4B), g-C$_3$N$_4$ QDs (Fig. 4C) and the primers (Fig. 4D) were 15 mg/mL, 18 mg/mL, 20 mg/mL and 15 μg/mL, respectively. 7.0 was the optimal pH (Fig. 4E).

In this work, the different concentrations of pcDNA3-HBV could be

detected by monitoring the photocurrent signal of the PEC biosensor under the optimum experimental conditions. The photocurrent decreased with the increasing concentration of pcDNA3-HBV as shown in Fig. 5A, B and C. The decrement of the photocurrent was proportional to the logarithm of the pcDNA3-HBV concentration ranging from 0.01 fmol/L to 20 nmol/L with a correlation coefficient of 0.9949. The regression equation was ΔI (μA) $=6.036+1.194 \lg c_{pcDNA3\text{-}HBV}$ (pmol/L). The limit of detection (LOD) was 0.005 fmol/L. The outstanding

sensitivity maybe resulted from the novel signal amplification strategy of the proposed PEC biosensor. And also the sensitization of N-GQDs and g-C$_3$N$_4$ QDs to TiO$_2$ NPs was attributed to good separated excitation energy and exiton conversion efficiency.

3.5. Selectivity, stability and reproducibility

The stability of the biosensor was also inspected in this work. As shown in Fig. 5D, the photocurrent response was recorded under more than 30 on/off irradiation cycles and no noticeable variation occurred, indicating the stable readout for signal collection. For the storage stability of the proposed biosensor after stored at 4 ºC for 14 days, 95% of the initial response was gained for the detection of 500 pmol/L pcDNA3-HBV, indicating the satisfactory storage stability of the developed biosensor.

To investigate the specificity of the proposed biosensor, some representative interfering substances involving pcDNA3, pcDNA3-His, pCMV5, pCMV-N-HA and pCMV-C-HA were selected for the interference tests. In the tests, a constructed biosensor incubated only with 500 pmoL/L pcDNA3-HBV was tested as the contrast (sample 1, Fig. 5E). Sample 7 was incubated with more than five kinds of gene fragments, which displayed the possible cross-reaction could be ignored. And also the photocurrent response was consistent with the calibration curve in Fig. 5C (500 pmoL/L pcDNA3-HBV). The specificity of the biosensor was also evaluated by measuring the photocurrent responses of 1000 pmoL/L pcDNA3, pcDNA3-His, pCMV5, pCMV-N-HA and pCMV-C-HA along with 500 pmoL/L pcDNA3-HBV under the same experimental conditions, respectively. As shown in Fig. 5F, there was no remarkable signal increase when incubated higher concentration of non-target DNA fragments. The above results indicated that the specificity of the biosensor was suitable.

The reproducibility of the biosensor was also studied by both intra-assay and inter-assay relative standard deviation (RSD). Analyzed from the experimental results, the intra-assay RSDs were 2.3%, 3.1% and 2.6% towards 10, 30 and 50 nmol/L of pcDNA3-HBV. The inter-assay RSDs of 4.4%, 3.7% and 4.5% were obtained by measuring the same samples with five electrodes prepared independently at the same experiment conditions. The results indicated the acceptable reproducibility and precision of this biosensor.

The adding standard recovery was also carried out as shown in Table S1, the recoveries of the biosensor were 103% and 102% and the relative standard deviation (RSD) was 2.04% and 1.79%. Therefore, the fabricated biosensor could be satisfactorily applied to determination of pcDNA3-HBV.

4. Conclusions

In this study, TiO$_2$ NPs/N-GQDs/g-C$_3$N$_4$ QDs nanocomposite was utilized as the novel photoactive materials to develop the PEC biosensor to detect pcDNA3-HBV. The formation of TiO$_2$ NPs/N-GQDs/g-C$_3$N$_4$ QDs heterojunction could efficiently avoid the photogenerated electrons recombination, which promoted photo-to-current conversion. The introduced N-GQDs and g-C$_3$N$_4$ QDs could result in more effective separation of photogenerated electrons and further enhanced conversion efficiency. This proposed biosensor displayed a low detection limit of 0.005 fmol/L as well as a linear range from 0.01 fmol/L to 20 nmol/L. This novel strategy could afford a promising application in clinical diagnostics with good selectivity, high sensitivity, acceptable reproducibility and stability.

Acknowledgments

Appendix A. Supporting information

Supplementary data associated with this article can be found in the online version at doi:10.1016/j.bios.2016.12.059.

References

Abdullah-Al-Nahain, Lee, J.E., In, I., Lee, H., Lee, K.D., Jeong, J.H., Park, S.Y., 2013. Target delivery and cell imaging using hyaluronic acid-functionalized graphene quantum dots. Mol. Pharm. 10 (10), 3736–3744.

An, T., Tang, J., Zhang, Y., Quan, Y., Gong, X., Al-Enizi, A.M., Elzatahry, A.A., Zhang, L., Zheng, G., 2016. Photoelectrochemical conversion from graphitic C$_3$N$_4$ quantum dot decorated semiconductor nanowires. ACS Appl. Mater. Inter. 8 (20), 12772–12779.

Bae, S., Kim, H., Lee, Y., Xu, X., Park, J.S., Zheng, Y., Balakrishnan, J., Lei, T., Kim, H.R., Song, Y.I., 2010. Roll-to-roll production of 30-inch graphene films for transparent electrodes. Nat. Nanotechno. 5 (8), 574–578.

Baker, L.A., Lee, K.C.L., Jimenez, C.P., Alibhai, H., Chang, Y.M., Leckie, P.J., Mookerjee, R.P., Davies, N.A., Andreola, F., Jalan, R., 2015. Circulating microRNAs reveal time course of organ injury in a porcine model of acetaminophen-induced acute liver failure. Plos One 10 (5), e0128076.

Cao, S., Low, J., Yu, J., Jaroniec, M., 2015. ChemInform abstract: polymeric photocatalysts based on graphitic carbon nitride. Adv. Mater. 27 (13), 2150–2176.

Carlsson, J.M., 2008. A metal-free polymeric photocatalyst for hydrogen production from water under visible light. Nat. Mater. 8 (1), 76–80.

Cheng, C., Amini, A., Zhu, C., Xu, Z., Song, H., Wang, N., 2014. Enhanced photocatalytic performance of TiO$_2$-ZnO hybrid nanostructures. Sci. Reps. 4 (8), (4181-4181).

Ding, L.-L., Ge, J.-P., Zhou, W.-Q., Gao, J.-P., Zhang, Z.-Y., Xiong, Y., 2016. Nanogold-functionalized g-C$_3$N$_4$ nanohybrids for sensitive impedimetric immunoassay of prostate-specific antigen using enzymatic biocatalytic precipitation. Biosens. Bioelectron. 85, 212–219.

Duan, J., Chen, S., Jaroniec, M., Qiao, S.Z., 2015. Porous C$_3$N$_4$ nanolayers@N-graphene films as catalyst electrodes for highly efficient hydrogen evolution. ACS Nano 9 (1), 931–940.

Feng, Q., Shen, Y., Li, M., Zhang, Z., Zhao, W., Xu, J., Chen, H., 2016. Dual-wavelength electrochemiluminescence ratiometry aased on resonance energy transfer between Au nanoparticles Functionalized g-C$_3$N$_4$ nanosheet and Ru(bpy)$_3^{2+}$ for microRNA detection. Anal. Chem. 88 (1), 937–944.

Fujishima, A., Honda, K., 1972. Electrochemical photolysis of water at a semiconductor electrode. Nature 238 (238), 37–38.

Gao, P., Ma, H., Yang, J., Wu, D., Zhang, Y., Du, B., Fan, D., Wei, Q., 2015. Anatase TiO$_2$ based photoelectrochemical sensor for the sensitive determination of dopamine under visible light irradiation. New J. Chem. 39 (2), 1483–1487.

Ge, L., Han, C., Liu, J., 2011. Novel visible light-induced g-C$_3$N$_4$/Bi$_2$WO$_6$ composite photocatalysts for efficient degradation of methyl orange. Appl. Catal. B-Environ. 108–109 (0), 100–107.

Gupta, V., Chaudhary, N., Srivastava, R., Sharma, G.D., Bhardwaj, R., Chand, S., 2011. Luminscent graphene quantum dots for organic photovoltaic devices. J. Am. Chem. Soc. 133 (26), 9960–9963.

Han, Q., Bing, W., Jian, G., Cheng, Z., Yang, Z., Zhang, Z., Qu, L., 2016. Atomically thin mesoporous nanomesh of graphitic C$_3$N$_4$ for high-efficiency photocatalytic hydrogen evolution. ACS Nano 10 (2), 2745–2751.

Hong, Y., Jiang, Y., Li, C., Fan, W., Xu, Y., Ming, Y., Shi, W., 2016. In-situ synthesis of direct solid-state Z-scheme V$_2$O$_5$/g-C$_3$N$_4$ heterojunctions with enhanced visible light efficiency in photocatalytic degradation of pollutants. Appl. Catal. B-Environ. 180, 663–673.

Jemal, A., Bray, F., Center, M.M., Ferlay, J., Ward, E., Forman, D., 2011. Global cancer statistics. Ca Cancer J. Clin. 61 (2), 69–90.

Jun, Y., Lee, E., Wang, X., Hong, W., Stucky, G., Thomas, A., 2013. From melamine-cyanuric acid supramolecular aggregates to carbon nitride hollow spheres. Adv. Funct. Mater. 23 (29), 3661–3667.

Kanan, M.W., Nocera, D.G., 2008. In situ formation of an oxygen-evolving catalyst in neutral water containing phosphate and Co^{2+}. Science 321 (5892), 1072–1075.

Kurbanov, F., Tanaka, Y., Mizokami, M., 2010. Geographical and genetic diversity of the human hepatitis B virus. Hepatol. Res. 40 (1), 14–30.

Lalwani, G., Sundararaj, J.L., Schaefer, K., Button, T., Sitharaman, B., 2014. Synthesis, characterization, in vitro phantom imaging, and cytotoxicity of A novel graphene-based multimodal magnetic resonance imaging X-Ray computed tomography contrast agent. J. Mater. Chem. 2 (22), 3519–3530.

Li, G., Lian, Z., Wang, W., Zhang, D., Li, H., 2016. Nanotube-confinement induced size-controllable g-C$_3$N$_4$ quantum dots modified single-crystalline TiO$_2$ nanotube arrays for stable synergetic photoelectrocatalysis. Nano Energy 19, 446–454.

Li, R., Liu, Y., Li, X., Zhang, S., Wu, D., Zhang, Y., Wei, Q., Du, B., 2014a. A novel multi-amplification photoelectrochemical immunoassay based on copper(II) enhanced polythiophene sensitized graphitic carbon nitride nanosheet. Biosens. Bioelectron. 62, 315–319.

Li, X., Zhu, S., Xu, B., Ma, K., Zhang, J., Yang, B., Tian, W., 2013. Self-assembled

graphene quantum dots induced by cytochrome c: a novel biosensor for trypsin with remarkable fluorescence enhancement. Nanoscale 5 (17), 7776–7779.

Li, X., Zhang, X., Ma, H., Wu, D., Zhang, Y., Du, B., Wei, Q., 2014b. Cathodic electrochemiluminescence immunosensor based on nanocomposites of semiconductor carboxylated g-C$_3$N$_4$ and graphene for the ultrasensitive detection of squamous cell carcinoma antigen. Biosens. Bioelectron. 55, 330–336.

Li, Y., Hu, Y., Zhao, Y., Shi, G., Deng, L., Hou, Y., Qu, L., 2011. An electrochemical avenue to green-luminescent graphene quantum dots as potential electron-acceptors for photovoltaics. Adv. Mater. 23 (6), 776–780.

Liu, W., Yan, X., Chen, J., Feng, Y., Xue, Q., 2013a. Novel and high-performance asymmetric micro-supercapacitors based on graphene quantum dots and polyaniline nanofibers. Nanoscale 5 (13), 6053–6062.

Liu, W.W., Feng, Y.Q., Yan, X.B., Chen, J.T., Xue, Q.J., 2013b. Superior Micro-Supercapacitors Based on Graphene Quantum Dots. Adv. Funct. Mate. 23 (33), 4111–4122.

Liu, Y., Xue, J.S., Zheng, T., Dahn, J.R., 1996. Mechanism of lithium insertion in hard carbons prepared by pyrolysis of epoxy resins. Carbon 34 (2), 193–200.

Liu, Y., Ma, H., Zhang, Y., Pang, X., Fan, D., Wu, D., Wei, Q., 2016. Visible light photoelectrochemical aptasensor for adenosine detection based on CdS/PPy/g-C$_3$N$_4$ nanocomposites. Biosens. Bioelectron. 86, 439–445.

Ma, W., Han, D., Zhou, M., Sun, H., Wang, L., Dong, X., Niu, L., 2014. Ultrathin g-C$_3$N$_4$/TiO$_2$ composites as photoelectrochemical elements for the real-time evaluation of global antioxidant capacity. Chem. Sci. 5 (10), 3946–3951.

Mortality, G.B.D.Co.D., C, 2015. Global, regional, and national age-sex specific all-cause and cause-specific mortality for 240 causes of death, 1990–2013: a systematic analysis for the Global Burden of Disease Study 2013. Lancet 385 (9963), 117–171.

Pan, D., Zhang, J., Li, Z., Wu, M., 2010. Hydrothermal route for cutting graphene sheets into blue-luminescent graphene quantum dots. Adv. Mater. 22 (6), 734–738.

Pang, X., Pan, J., Gao, P., Wang, Y., Wang, L., Du, B., Wei, Q., 2015. A visible light induced photoelectrochemical aptsensor constructed by aligned ZnO@CdTe core shell nanocable arrays/carboxylated g-C$_3$N$_4$ for the detection of proprotein convertase subtilisin/kexin type 6 gene. Biosens. Bioelectron. 74, 49–58.

Pang, X., Zhang, Y., Liu, C., Huang, Y., Wang, Y., Pan, J., Wei, Q., Du, B., 2016. Enhanced photoelectrochemical cytosensing of fibroblast-like synoviocyte cell based on visible light-activated ox-GQDs and carboxylated g-C$_3$N$_4$ sensitized TiO$_2$ nanorods. J. Mater. Chem. B 4, 4612–4619.

Peng, J., Gao, W., Gupta, B.K., Liu, Z., Romeroaburto, R., Ge, L., Song, L., Alemany, L.B., Zhan, X., Gao, G., 2012. Graphene quantum dots derived from carbon fibers. Nano Lett. 12 (2), 844–849.

Ponomarenko, L.A., Schedin, F., Katsnelson, M.I., Yang, R., Hill, E.W., Novoselov, K.S., Geim, A.K., 2008. Chaotic Dirac billiard in graphene quantum dots. Science 320 (5874), 356–358.

Tatematsu, K., Tanaka, Y., Kurbanov, F., Sugauchi, F., Mano, S., Maeshiro, T., Nakayoshi, T., Wakuta, M., Miyakawa, Y., Mizokami, M., 2009. A genetic variant of hepatitis B virus divergent from known human and ape genotypes isolated from a Japanese patient and provisionally assigned to new genotype. J. J. Virol. 83 (20), 10538–10547.

Tetsuka, H., Nagoya, A., Fukusumi, T., Matsui, T., 2016. Graphene quantum dots: molecularly designed, nitrogen-functionalized graphene quantum dots for optoelectronic devices. Adv. Mater. 28 (23), (4755-4755).

Tran, T.T., Trinh, T.N., Abe, K., 2008. New complex recombinant genotype of hepatitis B virus identified in Vietnam. J. Virol. 82 (11), 5657–5663.

Tsai, M.L., Tu, W.C., Tang, L., Wei, T.C., Wei, W.R., Shu, P.L., Chen, L.J., He, J.H., 2015. Efficiency enhancement of silicon heterojunction solar cells via photon management using graphene quantum dot as downconverters. Nano Lett. 16, 309–313.

Wang, C., Wu, Congyu, Zhou, Xuejiao, Han, Ting, Xin, Xiaozhen, Wu, Jiaying, Zhang, Jingyan, Guo, Shouwu, 2013a. Enhancing cell nucleus accumulation and DNA cleavage activity of anti-cancer drug viagraphene quantum dots. Sci. Reps. 3, 127–132.

Wang, G.L., Fang, X., Wu, X.M., Hu, X.L., Li, Z.J., 2016a. Label-free and ratiometric detection of nuclei acids based on graphene quantum dots utilizing cascade amplification by nicking endonuclease and catalytic G-quadruplex DNAzyme. Biosens. Bioelectron. 81, 214–220.

Wang, Q., Wang, W., Lei, J., Xu, N., Gao, F., Ju, H., 2013b. Fluorescence quenching of carbon nitride nanosheet through its interaction with DNA for versatile fluorescence sensing. Anal. Chem. 85 (24), 12182–12188.

Wang, S., Li, D., Sun, C., Yang, S., Guan, Y., He, H., 2014a. Synthesis and characterization of g-C$_3$N$_4$ /Ag$_3$VO$_4$ composites with significantly enhanced visible-light photocatalytic activity for triphenylmethane dye degradation. Appl. Catal. B-Environ. 144, 885–892.

Wang, W., Jimmy, C.Y., Shen, Z., Chan, D.K., Gu, T., 2014b. gC$_3$N$_4$ quantum dots: direct synthesis, upconversion properties and photocatalytic application. Chem. Commun. 50 (70), 10148–10150.

Wang, Y.-Z., Hao, N., Feng, Q.-M., Shi, H.-W., Xu, J.-J., Chen, H.-Y., 2016a. A ratiometric electrochemiluminescence detection for cancer cells using g-C$_3$N$_4$ nanosheets and Ag–PAMAM–luminol nanocomposites. Biosens. Bioelectron. 77, 76–82.

Wang, Y.-Z., Zhao, W., Dai, P.-P., Lu, H.-J., Xu, J.-J., Pan, J., Chen, H.-Y., 2016b. Spatial-resolved electrochemiluminescence ratiometry based on bipolar electrode for bioanalysis. Biosens. Bioelectron. 86, 683–689.

Yan, S.C., Lv, S.B., Li, Z.S., Zou, Z.G., 2010a. Organic-inorganic composite photocatalyst of g-C$_3$N$_4$ and TaON with improved visible light photocatalytic activities. Dalton Trans. 39 (6), 1488–1491.

Yan, X., Cui, X., Li, L.S., 2010b. Synthesis of large, stable colloidal graphene quantum dots with tunable size. J. Am. Chem. Soc. 132 (17), 5944–5945.

Yin, M., Li, Z., Kou, J., Zou, Z., 2009. Mechanism investigation of visible light-induced degradation in a heterogeneous TiO$_2$/eosin Y/rhodamine B system. Environ. Sci. Technol. 43 (21), 8361–8366.

Yoon, H., Chang, Y.H., Song, S.H., Lee, E.S., Jin, S.H., Park, C., Lee, J., Kim, B.H., Kang, H.J., Kim, Y.H., 2016. Intrinsic photoluminescence emission from subdomained graphene quantum dots. Adv. Mater. 28 (26), 5255–5261.

Zhang, J., Xiong, Z., Zhao, X., 2011. Graphene–metal–oxide composites for the degradation of dyes under visible light irradiation. J. Mater. Chem. 21 (11), 3634–3640.

Zhang, J., Zhang, M., Yang, C., Wang, X., 2014a. Nanospherical carbon nitride frameworks with sharp edges accelerating charge collection and separation at a soft photocatalytic interface. Adv. Mater. 26 (24), 4121–4126.

Zhang, X., Wang, H., Wang, H., Zhang, Q., Xie, J., Tian, Y., Wang, J., Xie, Y., 2014b. Single-layered graphitic-C$_3$N$_4$ quantum dots for two-photon fluorescence imaging of cellular nucleus. Adv. Mater. 26 (26), 4438–4443.

Zhang, Y., Wu, C., Zhou, X., Wu, X., Yang, Y., Wu, H., Guo, S., Zhang, J., 2013. Graphene quantum dots/gold electrode and its application in living cell H$_2$O$_2$ detection. Nanoscale 5 (5), 1816–1819.

Zhou, G., Zhao, Y., Zu, C., Manthiram, A., 2015a. Free-standing TiO$_2$ nanowire-embedded graphene hybrid membrane for advanced Li/dissolved polysulfide batteries. Nano Energy 12, 240–249.

Zhou, Z., Shen, Y., Li, Y., Liu, A., Liu, S., Zhang, Y., 2015b. Chemical cleavage of layered carbon nitride with enhanced photoluminescent performances and photoconduction. ACS Nano 9 (12), 12480–12487.

Zhu, S., Zhang, J., Tang, S., Qiao, C., Lei, W., Wang, H., Xue, L., Bo, L., Li, Y., Yu, W., 2012. Surface chemistry routes to modulate the photoluminescence of graphene quantum dots: from fluorescence mechanism to up-conversion bioimaging applications. Adv. Funct. Mater. 22 (22), 4732–4740.

Zou, J.P., Wang, L.C., Luo, J., Nie, Y.C., Xing, Q.J., Luo, X.B., Du, H.M., Luo, S.L., Suib, S.L., 2016. Synthesis and efficient visible light photocatalytic H$_2$ evolution of a metal-free g-C$_3$N$_4$ /graphene quantum dots hybrid photocatalyst. Appl. Catal. B-Environ. 193, 103–109.